PNAS
www.pnas.org

# Supplementary Information for

## A unified model for the dynamics of ATP-independent ultrafast contraction

**Carlos Floyd, Arthur T. Molines, Xiangting Lei, Jerry E. Honts, Fred Chang, Mary Williard Elting, Suriyanarayanan Vaikuntanathan, Aaron R. Dinner, M. Saad Bhamla**

**Corresponding Authors Mary Williard Elting, Suriyanarayanan Vaikuntanathan, Aaron R. Dinner, M. Saad Bhamla.**
**E-mails: mary.elting@ncsu.edu, svaikunt@uchicago.edu, dinner@uchicago.edu, saadb@chbe.gatech.edu**

### This PDF file includes:



### Other supplementary materials for this manuscript include the following:

Movies S1 to S3

## 1. Supplementary results

### A. Supplementary figures.

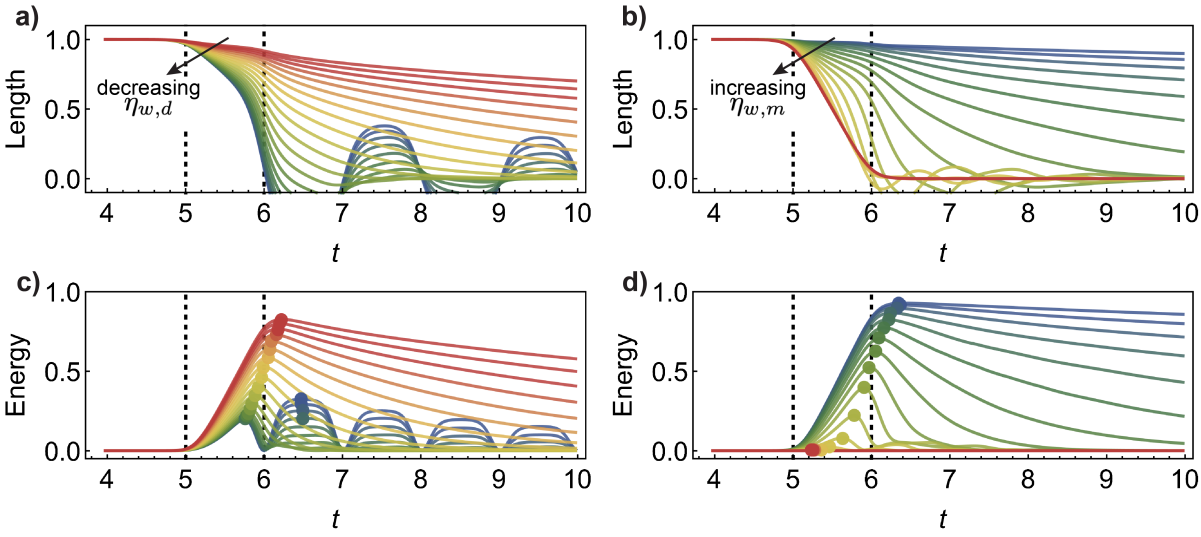


**Fig. S1. Dependence of length and energy trajectories on key timescales.** In panels (a) and (c), $\eta_{w,d}$ is varied from $0.25$ to $256$ in powers of $\sqrt{2}$ as the colors range from blue to red, with $\eta_{w,m} = 1$ fixed. The dimensionless length $\lambda(t)$ and energy $u_{\text{el}}(t)$ trajectories are shown; see the main text and $SI\ Appendix\ Supplementary\ methods$ Section E for a definition of $u_{\text{el}}$. The circles drawn in panel (c) show the values of $u_{\text{el}}^{\text{max}}$ which are used to compute $\chi$ in Figure 3e of the main text (see $SIAppendix$ Eq. (69)). Similarly, in panels (b), and (d), $\eta_{w,m}$ is varied from $0.0625$ to $32$ in powers of $\sqrt{2}$ as the colors range from blue to red, with $\eta_{w,d} = 2$ fixed.

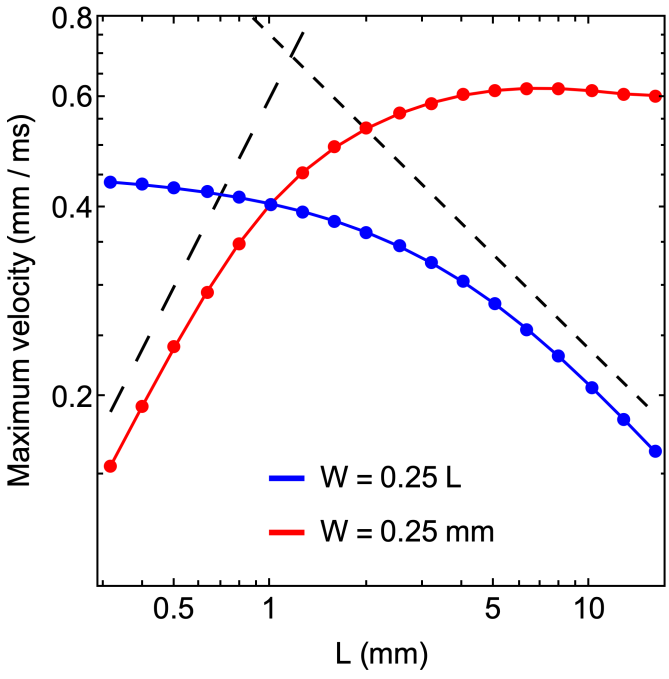


**Fig. S2. Coupling between length and width affects scaling.** In the dimensional model, Eq. (1) below, the maximum contraction rate $\dot{L}_{\text{max}} = \max_T |\partial_T L|$ is plotted as we vary the uncontracted length $L$. The red points correspond to conditions in which the width of the active stretch wave is fixed at $W = 0.25$ mm, while the blue points correspond to conditions in which the wave width scales with $L$ as $W = 0.25\ L$. The varying of $W$ with $L$ qualitatively changes the dependence of $\dot{L}_{\text{max}}$ on $L$. The remaining parameters used for this plot are $\alpha = 1$ (mm/ms)$^2$, $\mu = 3$ ms$^{-1}$, $V = 0.5$ mm/ms, and $g_{\text{min}} = 0$. The short and long dashed lines are proportional to $L^{-1/2}$ and $L$, respectively.

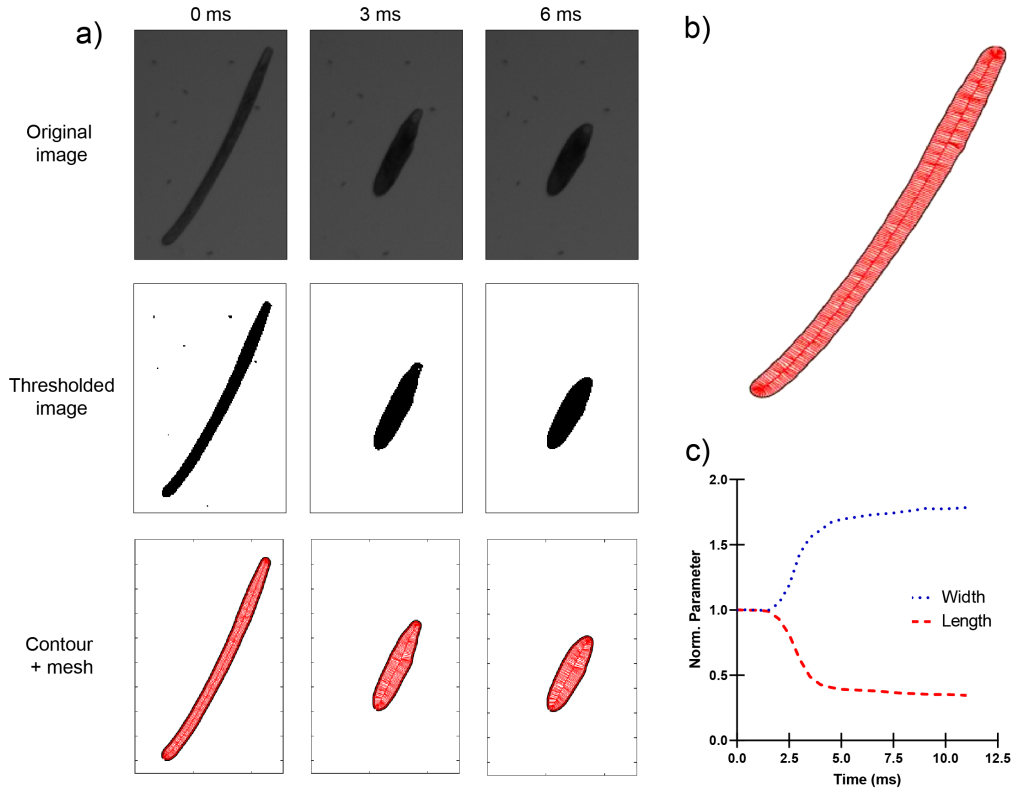


**Fig. S3. Measuring the length and width of *Spirostomum*.** (a) The original video image, the thresholded image, and the detected contours of *Spirostomum* at three moments during contraction. We used FijI (1) to threshold the images, and we used Matlab to run Morphometrics (2) with the pill-mesh option to obtain the cell contours. (b) Expanded view of the detected mesh to illustrate greater detail. The instantaneous width is reported as the median value of the width at several points along the organism's length, and the instantaneous length is reported as that of the central backbone curve. (c) Time course of the length and width, normalized by their initial values.

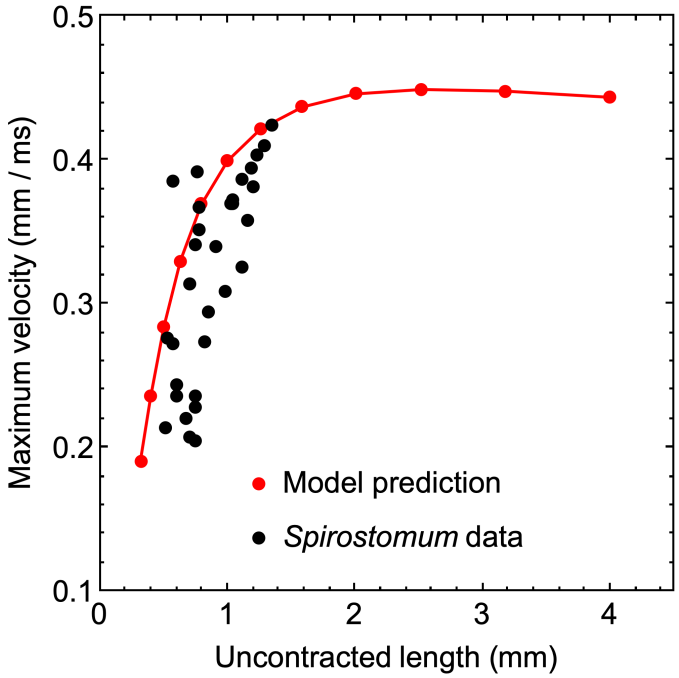


**Fig. S4. Experimental data for the dependence of contraction speed on initial length of *Spirostomum*.** Experimental data on the maximum contraction velocity is plotted against the initial length of the organism. The Pearson correlation coefficient is $0.72$ with a p-value of $5 \times 10^{-6}$ for this data set. The predicted scaling of maximum contraction velocity with length $L$ in the slow-wave limit of the model, Eq. (2) below, is plotted in red, using the parameters $V = 0.8$ m/s, $W = 0.2$ mm, $\mu/\alpha = 5$ (mm ms)$^{-1/2}$, and $g_{\min} = 0.4$ (cf. Table S1). See Ref. 3 for corresponding data on *Vorticella*.

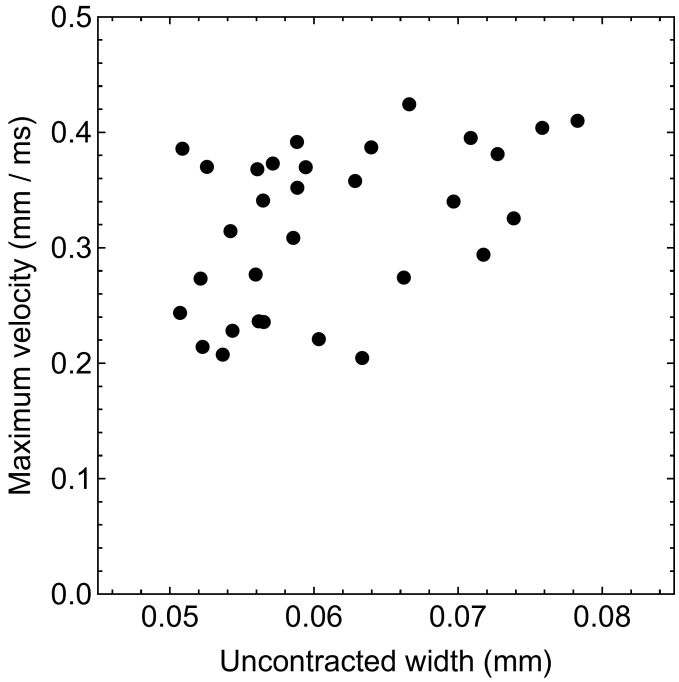


**Fig. S5. Experimental data for the dependence of contraction speed on initial width of *Spirostomum*.** Experimental data on the maximum contraction velocity is plotted against the initial width of the organism. The Pearson correlation coefficient is $0.44$ with a p-value of $0.013$ for this data set.

**B. Fitted parameters.** Here we fit the model to each of the five length trajectories for *Spirostomum* and *Vorticella* shown in Figure 2a and c of the main text. Figure S6 illustrates the fits to *Spirostomum*, and the fit parameters are given in Table S1. The contraction events occur close to the slow-wave limit of the model, in which inertia has nearly dropped out of the dynamics. Consequently, when fitting the full model, we found only the ratio of the parameters $\mu$ and $\alpha$ was constrained, and not their individual values. We thus fit the the curves in two ways. First, we fit the full model including inertia

$$\partial_T^2 X - \alpha\left(\partial_S^2 X - \partial_S g\right) + \mu \partial_T X = 0 \qquad [1]$$

by fixing $\alpha = 1$ and varying $\mu$, so that only the ratio $\alpha/\mu$ is varied independently. Second, we fit the slow-wave model

$$-\partial_S^2 X + \partial_S g + \frac{\mu}{\alpha}\partial_T X = 0 \qquad [2]$$

where the parameter $\mu/\alpha$ appears explicitly. We find that more consistent estimates of the model parameters can be obtained by fitting to the slow-wave model.

| Shared parameters | Sample 1 | Sample 2 | Sample 3 | Sample 4 | Sample 5 |
|---|---|---|---|---|---|
| $L$ (mm) | 0.61 | 0.58 | 0.52 | 0.51 | 0.76 |
| $g_{\min}$ | 0.45 | 0.35 | 0.37 | 0.37 | 0.38 |
| **Parameters for full model** | **Sample 1** | **Sample 2** | **Sample 3** | **Sample 4** | **Sample 5** |
| $V$ (mm/ms) | 0.8 | 0.8 | 0.8 | 0.85 | 0.9 |
| $W$ (mm) | 0.11 | 0.12 | 0.1 | 0.13 | 0.13 |
| $\mu/\alpha$ (ms/mm$^2$) | 25 | 28 | 45 | 40 | 14 |
| $\zeta = \alpha/V\mu L$ | 0.082 | 0.077 | 0.054 | 0.058 | 0.11 |
| **Parameters for slow-wave model** | **Sample 1** | **Sample 2** | **Sample 3** | **Sample 4** | **Sample 5** |
| $V$ (mm/ms) | 0.7 | 0.8 | 0.7 | 0.7 | 0.95 |
| $W$ (mm) | 0.14 | 0.18 | 0.2 | 0.2 | 0.15 |
| $\mu/\alpha$ (ms/mm$^2$) | 6 | 5 | 5 | 6 | 5 |
| $\zeta = \alpha/V\mu L$ | 0.390 | 0.431 | 0.549 | 0.467 | 0.277 |

**Table S1. Estimated parameters for *Spirostomum*.** The fitted model parameters for the five contraction samples are shown in Figure S6.

We next fit the five length trajectories of *Vorticella* shown in Figure 2c of the main text. Figure S7 illustrates these fits, and the fit parameters are given in Table S2.

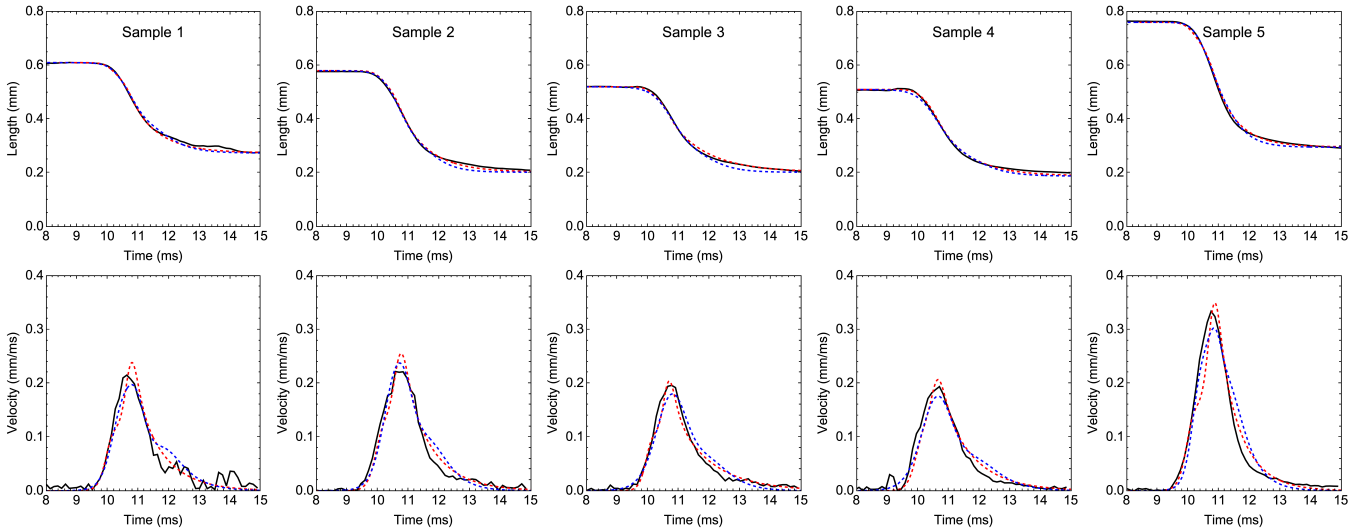


**Fig. S6. Fits for *Spirostomum*.** Experimental trajectories of length and contraction rate are shown as black curves, and fitted model solutions are shown as dashed red (full model) and blue (slow-wave model) curves for the five samples in Figure 2a and b of the main text. Due to experimental limitations, we did not track which traces are from multiple contractions of the same organism versus from different organisms.

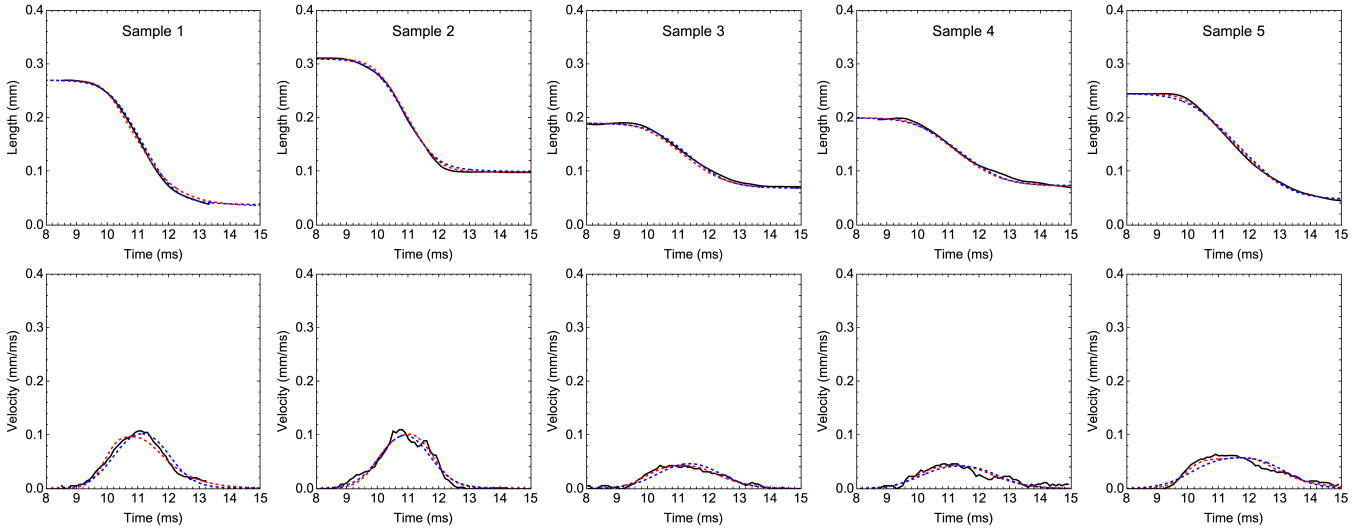


**Fig. S7. Fits for *Vorticella*.** Experimental trajectories of length and contraction rate are shown as black curves, and fitted model solutions are shown as dashed red (full model) and blue (slow-wave model) curves for the five samples in Figure 2c and d of the main text. Due to experimental limitations, we did not track which traces are from multiple contractions of the same organism versus from different organisms.

To validate these estimates of the parameters, we compare to the parameters reported in Ref. 4 which were used in a detailed computational model of *Vorticella* that achieved good agreement with experiments. We can compare our estimated value for $\mu/\alpha = \widetilde{\gamma}/F_{\mathrm{S}} = \gamma/F_{\mathrm{S}}L$ obtained from fitting to the slow-wave model to the corresponding quantity in Ref. 4, where $F_{\mathrm{S}}$ is the maximal contractile force generated by the myoneme fiber and $\widetilde{\gamma}$ is the drag constant of the organism $\gamma$ divided by its uncontracted length $L$. In their work, they use the estimate of $F_{\mathrm{S}} = 400$ nN measured in Ref. 5. To estimate the drag constant, we assume that drag is dominated by the contribution from the head (with diameter $D_{\mathrm{h}}$), which is subject to Stokes' law $\gamma = 3\pi D_{\mathrm{h}}\nu_{\mathrm{w}}$ where $\nu_{\mathrm{w}} = 10^{-3}$ Pa s is the viscosity of water. Using their estimate $L = 0.2$ mm, we obtain the value of $\mu/\alpha$ reported in Table S3. This comparison indicates reasonable agreement between our simplified description of the mechanics and a more detailed model.

We note that the importance of inertia can be estimated by comparing the maximal contraction rate ($\sim 0.1$ m/s for *Vorticella*) to the expected speed of sound $c_{\mathrm{s}}$ in the myoneme. As a lower bound for $\alpha = F_{\mathrm{S}}/A\rho$, we can estimate the cross-sectional area $A$ of the myoneme fiber as that of the whole stalk ($\sim 20\ \mu\mathrm{m}^2$) and we take the density of the material as that of water, $\rho = 1$ kg/m$^3$. With this, we find $\alpha \sim 20$ m$^2$/s$^2$ and $c_{\mathrm{s}} \approx 4.5$ m/s. A rough estimate of the speed of sound is thus at least an order of magnitude faster than the maximal contraction speed. This further suggests that for the conditions in which we measured contraction the organisms are in the slow-wave limit in which inertia can be neglected.

| Shared parameters | Sample 1 | Sample 2 | Sample 3 | Sample 4 | Sample 5 |
|---|---|---|---|---|---|
| $L$ (mm) | 0.27 | 0.31 | 0.19 | 0.20 | 0.24 |
| $g_{\min}$ | 0.13 | 0.32 | 0.36 | 0.36 | 0.18 |
| **Parameters for full model** | **Sample 1** | **Sample 2** | **Sample 3** | **Sample 4** | **Sample 5** |
| $V$ (mm/ms) | 0.3 | 0.23 | 0.13 | 0.13 | 0.13 |
| $W$ (mm) | 0.08 | 0.06 | 0.05 | 0.05 | 0.04 |
| $\mu/\alpha$ (ms/mm$^2$) | 30 | 15 | 45 | 45 | 40 |
| $\zeta = \alpha/V\mu L$ | 0.41 | 1.29 | 0.90 | 0.85 | 0.79 |
| **Parameters for slow-wave model** | **Sample 1** | **Sample 2** | **Sample 3** | **Sample 4** | **Sample 5** |
| $V$ (mm/ms) | 0.15 | 0.2 | 0.1 | 0.08 | 0.08 |
| $W$ (mm) | 0.06 | 0.08 | 0.05 | 0.04 | 0.04 |
| $\mu/\alpha$ (ms/mm$^2$) | 2 | 1 | 1 | 3 | 4 |
| $\zeta = \alpha/V\mu L$ | 12.34 | 16.13 | 52.63 | 20.83 | 12.75 |

**Table S2. Estimated parameters for *Vorticella*.** The fitted model parameters for the five contraction samples are shown in Figure S7.

| Parameter | Present study | Ref. 4 |
|---|---|---|
| $L$ (mm) | $0.25 \pm 0.05$ | 0.2 |
| $g_{\min}$ | $0.27 \pm 0.11$ | 0.25 |
| $V$ (mm/ms) | $0.12 \pm 0.05$ | 0.1 |
| $\mu/\alpha$ (ms/mm$^2$) | $2.2 \pm 1.3$ | 5.9 |

**Table S3. Estimated parameters for *Vorticella*.** The values reported for this study represent the mean and standard deviation of the five samples in Table S2.

## 2. Supplementary methods

**A. Derivation of continuum model.** Here we derive the continuum model of myoneme contraction, Eq. (2) in the main text. We treat the system as a one-dimensional chain of springs with open boundary conditions (or one end fixed for *Vorticella*) and non-autonomous rest lengths for each spring. We consider a set of $N$ masses connected by $N-1$ springs, where the force on the $i^{\text{th}}$ mass is given by

$$m\partial_T^2 X_i = k\left(X_{i+1} - X_i - G_{i+\frac{1}{2}}\right) - k\left(X_i - X_{i-1} - G_{i-\frac{1}{2}}\right) - \gamma\partial_T X_i. \quad [3]$$

Here, $m$ is the mass, $X_i(T)$ is the horizontal position of mass $i$, $T$ is time, $k$ is the stiffness of every spring, $G_{i+\frac{1}{2}}(T)$ is the current rest length of the spring connecting masses $i$ and $i+1$, and $\gamma$ is the drag coefficient. We use capital letters for dimensional variables and lowercase letters for dimensionless variables. To pass to a continuum description, we label the material coordinate $S$ and let the positions $X_i$ and $X_{i+1}$ be separated by a material distance $\delta$ which is assumed equal to the initial rest length $G_{i+\frac{1}{2}}(0)$ for each $i$. The original material length is $L$, so that $\delta = L/(N-1)$. We can rewrite Eq. (3) as

$$\begin{aligned} m\partial_T^2 X(S,T) = k\Big(& X(S+\delta,T) - X(S,T) - G\left(S+\frac{\delta}{2},T\right) \\ & + X(S-\delta,T) - X(S,T) + G\left(S-\frac{\delta}{2},T\right)\Big) - \gamma\partial_T X(S,T). \end{aligned} \quad [4]$$

We next assume $\delta$ is small and expand around $X(S,T)$ and $G(S,T)$. To second order in $\delta$, this gives (suppressing the dependence on $S$ and $T$ for clarity)

$$\begin{aligned} m\partial_T^2 X &= k\Big(X + \delta\partial_S X + \frac{1}{2}\delta^2\partial_S^2 X - X - G - \frac{1}{2}\delta\partial_S G - \frac{1}{8}\delta^2\partial_S^2 G \\ &\quad + X - \delta\partial_S X + \frac{1}{2}\delta^2\partial_S^2 X - X + G - \frac{1}{2}\delta\partial_S G + \frac{1}{8}\delta^2\partial_S^2 G\Big) - \gamma\partial_T X \\ &= k\left(\delta^2\partial_S^2 X - \delta\partial_S G\right) - \gamma\partial_T X. \end{aligned} \quad [5]$$

We switch to the dimensionless quantity $g(S,T) = G(S,T)/\delta$ representing the instantaneous rest length $G$ divided by the material distance $\delta$, which we call the active stretch. This gives

$$m\partial_T^2 X = k\delta^2(\partial_S^2 X - \partial_S g) - \gamma\partial_T X. \quad [6]$$

Next we introduce the constants $\widetilde{k} = k\delta$, $\widetilde{m} = m/\delta$, and $\widetilde{\gamma} = \gamma/\delta$, which represent how the stiffness, mass, and drag coefficient physically scale with the discretization length $\delta$, and then take the limit $\delta \to 0$ such that all third and higher order terms in the expansion vanish. This gives

$$\partial_T^2 X - \alpha\left(\partial_S^2 X - \partial_S g\right) + \mu \partial_T X = 0 \quad [7]$$

where $\alpha = \widetilde{k}/\widetilde{m}$ and $\mu = \widetilde{\gamma}/\widetilde{m} = \gamma/m$. The parameter $\alpha$ has units of velocity squared, and the parameter $\mu$ has units of inverse time.

We assume that at $T = 0$ the length of the organism linearly increases up to its undeformed material length, such that

$$X(S, 0) = S. \quad [8]$$

We also let it be at rest initially, such that

$$\partial_T X(S, 0) = 0. \quad [9]$$

We next consider the boundary conditions for Eq. (7) at the edges of the domain, $S = 0,\ L$. In the case of *Spirostomum*, we take stress-free boundary conditions at both ends, while for *Vorticella* we use the stress-free condition at $S = 0$ and the Dirichlet condition $X(L, T) = L$. To derive the stress-free boundary condition, we repeat the discretization steps given above at the mass $i = 0$. We start with

$$m\partial_T^2 X_0 = k\left(X_1 - X_0 - G_{\frac{1}{2}}\right) - \gamma \partial_T X_0, \quad [10]$$

and, passing to the continuous material coordinate $S$,

$$m\partial_T^2 X(0, T) = k\left(X(\delta, T) - X(0, T) - G\left(\frac{\delta}{2}, T\right)\right) - \gamma \partial_T X(0, T). \quad [11]$$

Upon expanding with respect to $\delta$, we find (again dropping explicit argument dependence)

$$m\partial_T^2 X = k\left(\delta \partial_S X + \frac{1}{2}\delta^2 \partial_S^2 X - G - \frac{1}{2}\delta \partial_S G - \frac{1}{8}\delta^2 \partial_S^2 G\right) - \gamma \partial_T X. \quad [12]$$

Introducing again $\alpha$, $\mu$, and $g$, we have

$$\partial_T^2 X = \alpha\left(\frac{1}{\delta}\partial_S X + \frac{1}{2}\partial_S^2 X - \frac{1}{\delta} g - \frac{1}{2}\partial_S g - \frac{1}{8}\delta^2 \partial_S^2 g\right) - \mu \partial_T X. \quad [13]$$

Taking the limit $\delta \to 0$ leaves us with the following condition at $S = 0$:

$$\partial_S X(0, T) = g(0, T). \quad [14]$$

Note that the drag and inertial contributions to the force balance have not survived the limit in this case because the terms proportional to $\partial_S X$ and $g$ do not cancel out in the expansion as they did in Eq. (5), and these terms dominate as $\delta \to 0$. Through the same steps (or by symmetry considerations), we obtain an identical stress-free condition applying at $S = L$.

## B. Description of $Ca^{2+}$ model.

***B.1. Review of $Ca^{2+}$ models.*** There is a wide range of mathematical models that describe the time and space-dependent dynamics of intracellular $Ca^{2+}$, reviewed in Refs. 6 and 7. These dynamics are quite varied, including concentration patterns that are homogeneous in space but oscillatory in time, outward-propagating spirals, and the fast-traveling wavefronts which underlie mechanical contraction in *Spirostomum* and *Vorticella* (4, 8–11). An important process giving rise to these dynamics is calcium-induced calcium release (CICR), in which binding of $Ca^{2+}$ to $IP_3$ and ryanodine receptor calcium channels causes them to release additional $Ca^{2+}$. This positive feedback does not continue indefinitely, as the probability of the channel being open (and hence its release rate) has a bell-shaped dependence on the logarithm of bound $Ca^{2+}$ (6). This dual role of $Ca^{2+}$ inducing and subsequently inhibiting the channel release gives rise to the oscillatory patterns observed at long timescales. For computing the speed and width of the traveling wave front in our case, however, it is sufficient to consider only the positive feedback.

Models of $Ca^{2+}$ dynamics differ widely in their complexity, with the number of free parameters ranging from just a handful to more than a hundred (6). Key features that distinguish $Ca^{2+}$ models include:

- The number of separate species tracked (i.e., just cytosolic $Ca^{2+}$ or also endoplasmic reticulum $Ca^{2+}$ and intermediate signaling molecules like $IP_3$)
- Whether the channels are modeled as continuously or discretely distributed (with the latter choice found in the "fire-diffuse-fire" models (12, 13))
- The level of detail for the CICR kinetics of $Ca^{2+}$ channels, which are multimeric molecules that cooperatively bind $Ca^{2+}$ and signaling molecules

With the goal in mind of constructing a minimal model of *Spirostomum* and *Vorticella*, and given the scarcity of experimentally measured kinetic parameters for these systems, we consider a highly simplified model which allows for traveling wave solutions and has clear interpretable parameters. Additionally, we opt for a continuous distribution of $Ca^{2+}$ receptors (rather than a discrete fire-diffuse-fire description), as it is significantly more tractable. In the fire-diffuse-fire models, the continuous case is formally obtained as a limit of the discrete case when the release rate of $Ca^{2+}$ is rate-limiting rather than the inter-receptor diffusion time (12, 13).

***B.2. Kuperfman model.*** For these reasons, we use the Kupferman model of Ref. 14 as the basis for our analysis of $Ca^{2+}$ dynamics and its mechanical effects in *Spirostomum* and *Vorticella*. It tracks the cytosolic $Ca^{2+}$ concentration as a function of time $T$ and one space dimension $S$. Below, we also consider the concentration of myoneme-bound $Ca^{2+}$. In the laboratory frame, the reaction-diffusion dynamics for the cytosolic $Ca^{2+}$ concentration $C$ are

$$\partial_T C = D_C \partial_S^2 C - \Gamma C + J\Theta(C - C_0). \quad [15]$$

Here, $D_C$ is the $Ca^{2+}$ diffusion constant in the cytosol, $\Gamma$ is the first-order rate constant for $Ca^{2+}$ leakage out of the cytosol, $J$ is the rate of $Ca^{2+}$ release by the open channels, and $C_0$ is the threshold concentration for the channel to open and begin releasing $Ca^{2+}$. Note that in this model of CICR, all of the complexity of cooperative binding of $Ca^{2+}$ to the channels, dependence on local signaling molecule concentrations, and later inhibition of release is removed by assuming that the release rate dependence on $Ca^{2+}$ concentration is captured by a Heaviside function $\Theta(C - C_0)$ (rather than some non-monotonic function which would be necessary to describe the dynamics on a longer timescale).

Eq. (15) is rescaled in two steps: first, we non-dimensionalize and we then shift to the frame that is moving together with the traveling wave. The new non-dimensional variables $c$, $t$, and $s$ are introduced by expressing concentration in units of $C_u \equiv C_0$, time in units of $T_u \equiv C_0/J$, and length in units of $S_u = \sqrt{C_0 D_C/J}$. The traveling frame is found by introducing the variable $u = s - vt$, where the traveling wave speed $v$ is expressed in units of $V_u = \sqrt{JD_C/C_0}$. With this rescaling, Eq. (15) becomes

$$\partial_u^2 c + v\partial_u c - \xi c + \Theta(c - 1) = 0, \quad [16]$$

where $\xi \equiv C_0\Gamma/J$.

Eq. (16) can be solved exactly, which is a key benefit of the Kupferman model (14). The solution is

$$c(u) = \begin{cases} \frac{1}{\xi} + \frac{\xi - 1}{\xi} e^{q^+ u} & u < 0 \\ e^{q^- u} & u > 0, \end{cases} \quad [17]$$

where

$$q^{\pm} = \frac{1}{2}\left(-v \pm \sqrt{v^2 + 4\xi}\right) \quad [18]$$

and

$$v = \frac{1 - 2\xi}{\sqrt{1 - \xi}}. \quad [19]$$

The point $u = 0$ is the boundary between the open ($u > 0$) and closed ($u < 0$) channels, such that at $u = 0$ we have $c = 1$. To obtain this solution to the ODE Eq. (16) on the domains $(-\infty, 0)$ and $(0, \infty)$, the free constants were determined by the matching conditions $c(0^-) = c(0^+) = 1$ and $\partial_u c(0^-) = \partial_u c(0^+)$.

***B.3. Width of myoneme-bound $Ca^{2+}$ profile.*** We next extend the Kufperman model by introducing the concentration $B(S, T)$ of $Ca^{2+}$ bound to myoneme proteins. Let $B_{\text{tot}}$ be the conserved total concentration of myoneme binding sites, which is spatially uniform. When calcium totally saturates the available binding sites on myoneme, then $B = B_{\text{tot}}$. The new reaction-diffusion dynamics for $C$ and $B$ are

$$\partial_T C = D_C \partial_S^2 C - \Gamma C + J\Theta(C - C_0) - K_+ C(B_{\text{tot}} - B) + K_- B \quad [20]$$

$$\partial_T B = K_+ C(B_{\text{tot}} - B) - K_- B. \quad [21]$$

Here $K_+$ is the dimensional binding rate and $K_-$ is the dimensional unbinding rate. We have assumed that the bound $Ca^{2+}$ does not diffuse. By numerically integrating Eq. (20) and Eq. (21), we observed that the traveling profile of $B$ has a width that depends on several factors including the binding rate $K_+$ (see Figure S9 below). The width in turn affects the width of the stretch profile $g$, which can be modeled as a linear function of $B$. The width of the stretch profile $g$ is an important feature governing the contraction dynamics in the mechanical model (see Figure 2e in the main text). Our goal here is to study how the width of the $B$ profile depends on the kinetic parameters in Eq. (20) and Eq. (21).

The rescaled versions of these equations are

$$\partial_u^2 c + v\partial_u c - \xi c + \Theta(c - 1) - k_+ c(b_{\text{tot}} - b) + k_- b = 0 \quad [22]$$

$$v\partial_u b + k_+ c(b_{\text{tot}} - b) - k_- b = 0, \quad [23]$$

where $k_+ = K_+ C_0^2/J$, $k_- = K_- C_0/J$, $b = B/C_0$, and $b_{\text{tot}} = B_{\text{tot}}/C_0$. Unfortunately, Eq. (22) and Eq. (23) are analytically intractable due to the non-linearity from the binding reaction. We therefore look for an approximate solution by relying on two assumptions:

1. The total myoneme concentration $b_{\text{tot}}$ is sufficiently small that the dynamics of $c$ do not depend on $b$.

2. In the range over which $b$ is varying, around $u = 0$, the form of $c(u)$ is approximately linear.

Regarding the first assumption, we find numerically that increasing $b_{\mathrm{tot}}$ introduces small corrections to the predicted scaling behavior. Nonetheless, we can still gain insight into the model by assuming that the first assumption holds. Regarding the second assumption, we can check graphically that the profile of $c$ is indeed roughly linear over the range where $b$ is changing (although this also breaks down if $b_{\mathrm{tot}}$ is large). The linear approximation to $c(u)$ around $u = 0$ is

$$c(u) \approx 1 + \frac{\xi - 1}{\xi} q_+ u = 1 - u\sqrt{1-\xi}. \quad [24]$$

This holds for both sides of the piecewise definition in Eq. (17) since the derivatives are matched at $u = 0$. In this approximation, $c(u)$ goes to zero at $u_0 = 1/\sqrt{1-\xi}$, and since $b$ cannot be greater than zero if $c = 0$, then $b$ must go to zero at that point as well.

With these assumptions the dynamics are reduced to

$$v\partial_u b + k_+(1 - u\sqrt{1-\xi})(b_{\mathrm{tot}} - b) - k_- b = 0 \quad [25]$$

which admits an exact solution:

$$\frac{b(u)}{b_{\mathrm{tot}}} = 1 + A \exp\left(\frac{2(k_- + k_+)u - mk_+u^2}{2v}\right) + \frac{\sqrt{2}k_-}{n}\mathrm{daw}\left(\frac{k_- + k_+ - mk_+ s}{\sqrt{2}n}\right). \quad [26]$$

Here, $m = \sqrt{1-\xi}$ and $n = \sqrt{mk_+ v}$, and daw is the Dawson function, defined as

$$\mathrm{daw}\,(x) = e^{-x^2}\int_0^x e^{t^2} dt. \quad [27]$$

The constant $A$ can be fixed by requiring $b(u_0) = 0$, resulting in

$$\frac{b(u)}{b_{\mathrm{tot}}} = 1 + \left(\frac{\sqrt{2}k_-}{n}\mathrm{daw}\left(\frac{k_-}{\sqrt{2}n}\right) - 1\right)\exp\left(\frac{2(k_- + k_+)u - mk_+u^2}{2v}\right) - \frac{\sqrt{2}k_-}{n}\mathrm{daw}\left(\frac{k_- + k_+ - mk_+u}{\sqrt{2}n}\right). \quad [28]$$

This is defined for $u < u_0$, while for $u \geq u_0$, $b(u) = 0$. Eq. (28) can be simplified because $k_-/n \ll 1$ for typical values of the parameters, while the Dawson function does not exceed 1 in absolute value. We can thus write

$$\frac{b(u)}{b_{\mathrm{tot}}} \approx 1 - \exp\left(\frac{2(k_- + k_+)u - mk_+u^2}{2v}\right). \quad [29]$$

Furthermore, the quadratic part of the exponent dominates after rescaling back to dimensional units, allowing us to finally write

$$\frac{b(u)}{b_{\mathrm{tot}}} \approx 1 - \exp\left(-\frac{mk_+u^2}{2v}\right). \quad [30]$$

In Figure S8 we compare Eq. (28), Eq. (29), and Eq. (30) for typical values of the parameters.

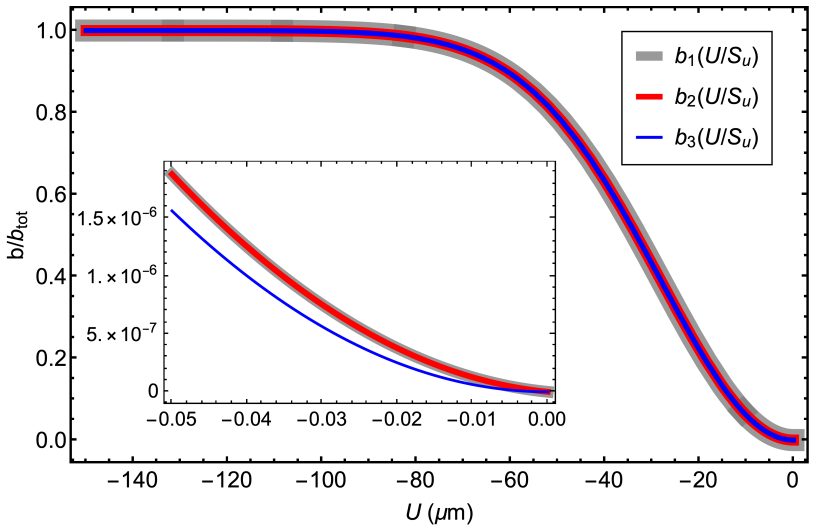


**Fig. S8. Comparison of Eqs. (28), (29), and (30).** For the parameters in Table S4, we show the three equations for $b(u)$, where $b_1(u)$ refers to Eq. (28), $b_2(u)$ refers to Eq. (29), and $b_3(u)$ refers to Eq. (30). For these parameters, $S_u = \sqrt{C_0 D_C/J} \approx 0.003$. The inset show the region close to the origin, where $b_3(u)$ visibly differs from $b_1(u)$ and $b_2(u)$.

Eq. (30) is a Gaussian function of $u$ with a width given by $w = \sqrt{v/mk_+}$. Assuming $m \approx 1$ since $\xi$ is typically small, in dimensional units we have

$$\frac{k_+ u^2}{v} = W^{-2}(S - VT)^2 \quad [31]$$

where

$$W^{-2} = \frac{K_+}{V}\sqrt{\frac{C_0 J}{D_C}}. \quad [32]$$

We can simplify using the fact that $V \approx \sqrt{JD_C/C_0}$ (i.e., $v \approx 1$) since $\xi$ is small in Eq. (19) and, by assumption, the dynamics of $c$ do not depend on $b$. This gives the final result

$$W \approx \sqrt{\frac{D_C}{C_0 K_+}}. \quad [33]$$

Eq. (33) predicts that the width $W$ only depends on the three quantities $D_C, C_0$, and $K_+$. We confirm this numerically in the next section.

An interesting extension to the model, which we leave to future work, would be to introduce tension-gated $Ca^{2+}$ channels in the chemical dynamics, to allow for two-way coupling between chemistry and mechanics (15). This kind of mechanochemical coupling would allow for additional dynamical features like pattern formation, limit cycles, or damped oscillations without requiring inertia. Related work on the mechanochemical dynamics of elastic media can be found, for instance, in Refs. 16 and 17. Another potential extension is to consider a finite delay between $Ca^{2+}$ binding and rest length shrinking, which would introduce an additional timescale to the model. However, we have not addressed this possibility in our current work. Furthermore, we have not explored the possibility that $Ca^{2+}$ binding could alter the local stiffness of the myonemes.

***B.4. Numerical results.*** We demonstrate through numerical tests the accuracy of the above scaling form for $W$, Eq. (33). Throughout this section and in the inset of Figure 2e in the main text, we use the parameters in Table S4 unless noted otherwise. These parameters are mostly in keeping with those used in Ref. 14 except for $K_+$ and $K_-$, which are based on values roughly inferred for *Vorticella* from Ref. 4.

| Symbol | Value | Units |
|---|---|---|
| $D_C$ | 200 | $\mu m^2/s$ |
| $C_0$ | 0.5 | $\mu M$ |
| $\Gamma$ | 100 | $1/s$ |
| $J$ | $10^7$ | $\mu M/s$ |
| $K_+$ | 0.5 | $1/\mu M\ s$ |
| $K_-$ | 0.15 | $1/s$ |
| $B_{tot}$ | 1000 | $\mu M$ |

**Table S4. Kinetic parameters of the $Ca^{2+}$ model.**

Using the methods described in *Materials and methods* section C of the main text, we numerically integrate the full chemical dynamics, Eq. (20) and Eq. (21), on a domain of length $L = 1000$ $\mu$m for 0.05 s, and we use the boundary condition $\partial_S C(0,T) = \partial_S C(L,T) = 0$. We initiate the wave by setting $C(S,0) = J/\Gamma$ on the segment $S \in [0,100]$ and $B(S,0) = 0$ everywhere. To obtain $W$ and test the predicted scaling form in Eq. (33), we fit to the profile $B(S, 0.005\text{ s})$ the sigmoidal function

$$B_{\text{fit}}(S) = 1 - \frac{1}{1 + e^{-\frac{S-O}{W}}} \quad [34]$$

for the offset $O$ and width $W$. Note that this functional form does not match the derived form in Eq. (30) but nonetheless has a well-defined characteristic width. We favor using the sigmoidal approximation to the bound concentration profile because it does not involve a piecewise definition as the form in Eq. (30) does (where $b(u) = 0$ for $u \geq 0$), making it much easier to work with. If the derived scaling is observed for the width of this function, it suggests that the width's scaling behavior does not depend on the specific functional form in Eq. (30).

In Figure S9a we show the concentration profiles for $C$ and $B$ from $T = 0$ s to $T = 0.025$ s, illustrating the propagation of the diffusing and bound $Ca^{2+}$ profiles. We note that the step jump near $S = 100$ on the left of these plots is an artifact of our choice for initial conditions and does not play an important role in the mechanical model of contraction, where a traveling sigmoidal approximation to the bound calcium concentration is used. In Figure S9b we show these profiles at $T = 0.01$ s, along with the fit of Eq. (34) to $B(S)$. Note that the profile for $C$ is indeed approximately linear over the range where $B$ is changing, validating our previous assumption. We show similar profiles for the condition when $K_+ = 0.125$ $(\mu M\ s)^{-1}$ and $D_C = 800$ $\mu m^2/s$ (Figure S9c), and when $B_{tot} = 16,000$ $\mu$M (Figure S9d). In Figure S10 we show the scaling of $W$ with the quantities $K_+$, $K_-$, $D$, $C_0$, $\Gamma$, and $J$. We predict from Eq. (33) that the scaling exponents for these will be, respectively, $-1/2,\ 0,\ 1/2, -1/2,\ 0$, and 0, and these predictions are numerically confirmed.

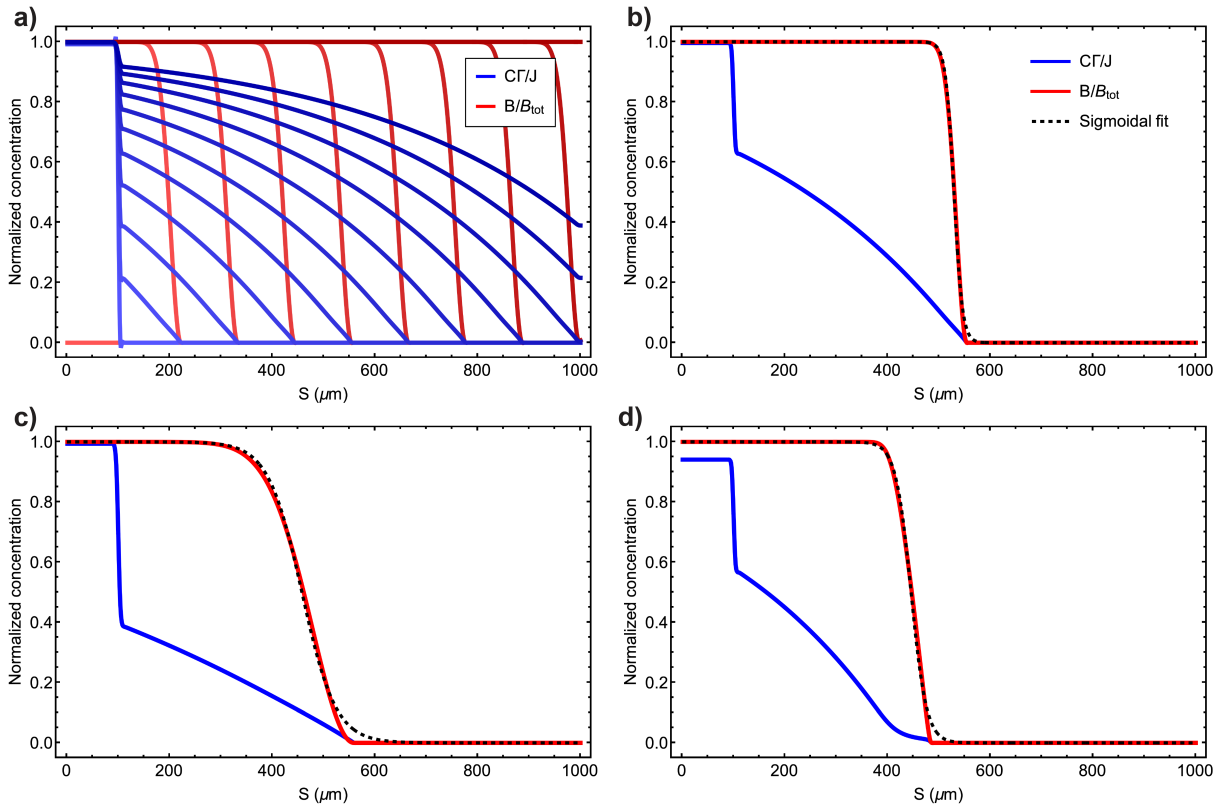


**Fig. S9. Numerical integration of** Eq. (20) **and** Eq. (21)**.** (a) The profiles of $C$ and $B$ from $T = 0$ s to $T = 0.025$ s in steps of $0.005$ s as brightness ranges from light to dark. (b) The profiles of $C$ and $B$ at $T = 0.01$ s. The fit of Eq. (34) to the profile of $B$ is shown as a dashed black line. The fitted width of $B$ is $8.2$ $\mu$m. (c) The profiles of $C$ and $B$ at $T = 0.001$ s for the same parameters as in (a) but with $K_+ = 0.125$ ($\mu$M/$s$) and $D_C = 800$ ($\mu$m$^2$/$s$). The fitted width of $B$ is $33.6$ $\mu$m. (d) The profiles of $C$ and $B$ at $T = 0.01$ s for the same parameters as in (a) but with $B_{\text{tot}} = 16,000$ $\mu$M. The fitted width of $B$ is $15.0$ $\mu$m.

**C. Model limitations and extensions.** The goal of the the model developed in this paper is to reproduce available experimental observations, such as asymmetrical contraction and the scaling of contraction speed with environmental viscosity, and yet still to be sufficiently simple that we can analytically study its behavior. To this end, we have abstracted several biophysical details into coarse-grained parameters, and we have kept only those features expected to play dominant roles in controlling the contraction speed. These retained features include the elasticity of the myonemes, the Stokes drag on the compression motion, and the dynamics of the chemical wave controlling the myoneme actuation. We have neglected possible volume or area conservation of the cells, spatial variation in the drag coefficient along the cell's length (4, 18), twisting dynamics or three-dimensional geometry of the cell bodies (4, 19), braking contributed by poroelasticity of the intracellular environment (20, 21) or entanglement of the internal organelles (22), elastic resistance by auxiliary elastic elements (19), and intermediate Reynolds number corrections to the viscous drag (4, 18). Detailed treatment of these neglected physical ingredients will likely require organism-specific considerations and numerical approaches, but in the remainder of this section we discuss how some of these features could be approximately included in our modeling framework. We emphasize the limits in which the extended models reduce to our minimal model, which clarifies our assumptions and why our minimal model can successfully capture organismal dynamics.

***C.1. Transverse deformation and twisting during contraction.*** We first consider additional deformation modes besides uniaxial compression. For instance, during contraction of *Spirostomum* there is appreciable twisting of the organism about its compression axis as well as heterogeneous variations in its transverse width. In *Vorticella*, the contraction force is localized to a thin myoneme fiber which wraps around a thicker elastic stalk. Contraction of the approximately one-dimensional myoneme fiber significantly deforms the stalk, pulling it from an initially straight conformation into a compressed helical conformation. A numerical model of this process based on the Cosserat rod theory has been studied in Ref. 4. Interestingly, it was found that the elasticity and dynamics of the stalk only marginally affects the projected one-dimensional compression dynamics, which are to a good approximation dominated by the drag on the large head at the end of the stalk.

Accurate modeling of non-compressional degrees of freedom depends on the specific myoneme arrangement and body plan of the organism under consideration, making it difficult to offer a general prescription for treating these effects. However, accounting for such modes is expected to improve quantitative accuracy since these modes can introduce timescales which may enter in the compression dynamics, depending on the parameter regime under consideration. Additionally, understanding the slow, active re-extension phase of these organisms likely requires detailed modeling of their geometry (see Ref. 4 for a study of

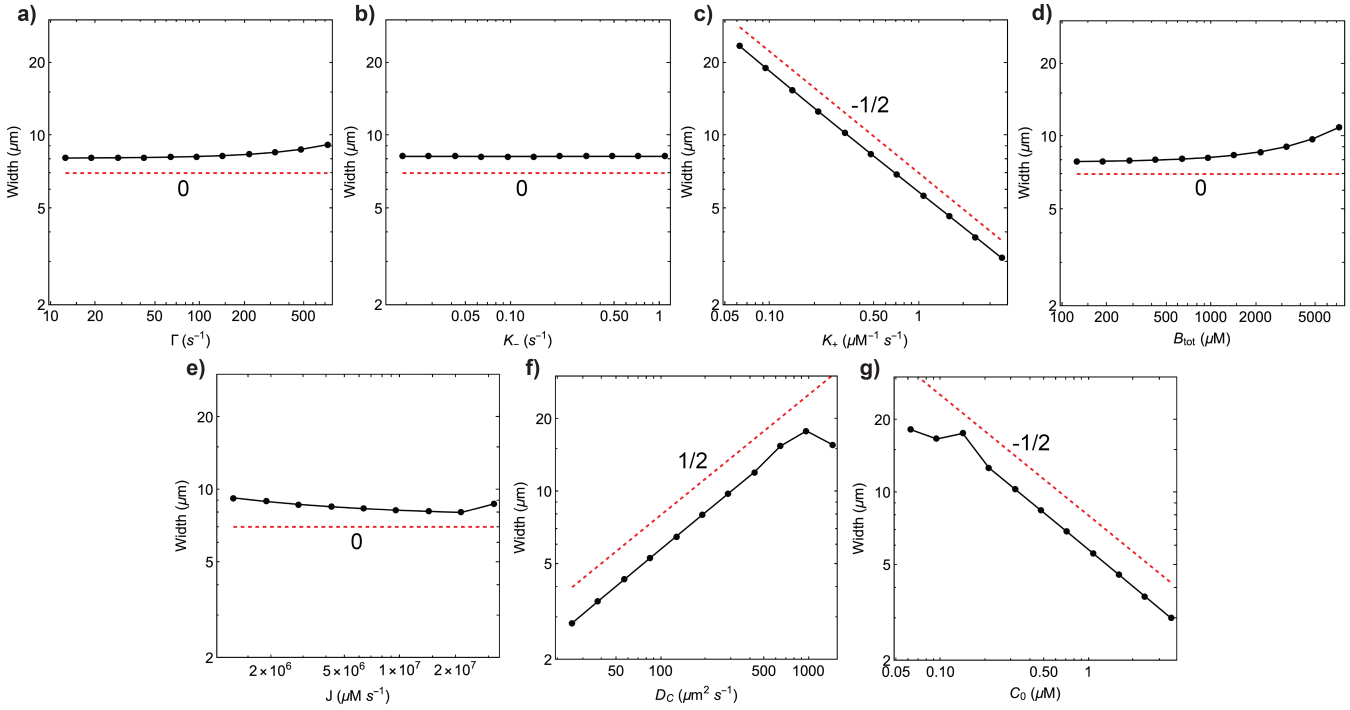


**Fig. S10. The scaling of $W$.** Results from fitting Eq. (34) to $B(S, 0.005\ \mathrm{s})$, obtained from numerical integration, shown as connected black dots. The red dotted lines illustrate the predicted scaling from the analytical result $W \approx \sqrt{D_C/C_0 K_+}$.

re-extension in *Vorticella*). Here, we focus on one deformation mode, which is the twisting during compression experienced by *Spirostomum*. We leave detailed studies of other geometrical aspects of myoneme contraction to future work, although in Section C.3 we discuss how some of these effects could be approximately treated as passive auxiliary springs which resist the active compression of myonemes.

In *Spirostomum*, a sheath of microtubules wraps around the organism (19, 23). We can view this sheath as a torsional elastic spring which resists twisting and compression. We introduce a variable $\Theta(S,T)$ describing the local angle that the cross-section makes with the compression axis. A quadratic elastic energy function for the $i^{\text{th}}$ connection the discrete chain can be written as

$$\begin{aligned} U_{\text{el},i} =& \frac{k}{2}\left(X_{i+1} - X_i - G_{i+\frac{1}{2}}\right)^2 + \frac{k^*}{2}\left(X_{i+1} - X_i - G^*_{i+\frac{1}{2}}\right)^2 \\ &+ \frac{k_\Theta}{2}\left(\Theta_{i+1} - \Theta_i - R_{i+\frac{1}{2}}\right)^2 + k_c\left(X_{i+1} - X_i - G^*_{i+\frac{1}{2}}\right)\left(\Theta_{i+1} - \Theta_i - R_{i+\frac{1}{2}}\right) \end{aligned} \quad [35]$$

where $G^*_{i+\frac{1}{2}}$ is the rest length of the microtubule sheath segment, $R_{i+\frac{1}{2}}$ is the equilibrium value of the twist, and $k_c$ captures an energetic coupling between twisting and stretching. We note that positivity of the energy requires setting $|k_c| < \sqrt{k_\Theta k^*}$ (24). This form for the energy is commonly used to model molecules such as DNA (25). Through steps analogous to those in the previous section, one can pass to a continuum limit of the dynamics of Eq. (35). Two new timescales are introduced, corresponding to the parameters $k_\Theta$ and $k_c$. We leave a study of this model to future work, but we note here that the model without twisting can be obtained as a limit of Eq. (35) in which the coupling constant $k_c$ is negligible. The magnitude of this coupling term tends to be much smaller than the stretching modulus (by a ratio of $\sim 1/10$ for DNA (25)) and can be omitted in the minimal model studied in this paper.

***C.2. Poroelasticity.*** Beyond twisting, an additional dynamical feature of *Spirostomum* contraction is the motion of the internal of fluid, whose possible volume conservation in the organism may produce motion transverse to the contraction direction (see Figure S3 and Ref. 19). Accurate treatment of this aspect of the dynamics requires specifying the poroelastodynamics of the fluid in the cell interior and boundary conditions that prevent its exit through the cell membrane (see, e.g., Ref. 17). While a full treatment of these dynamics is beyond the present study, we now describe a treatment of poroelasticity that provides an approximate understanding of the contribution of the fluid motion to the one-dimensional compression dynamics.

**Poroelastodynamic theory** Poroelasticity describes the mechanics of sponge-like materials that have a connected solid skeleton with pores that are filled with a fluid. Originally developed to describe the mechanics of water saturated soil (26, 27), it is known to introduce timescales in the dynamics of intracellular environments (20, 21), nastic plants (28, 29), and muscles (17). To treat the effects of poroelasticity on the contraction dynamics of myoneme networks, we build on the linear poroelastodynamic theory outlined in Refs. 30 and 31.

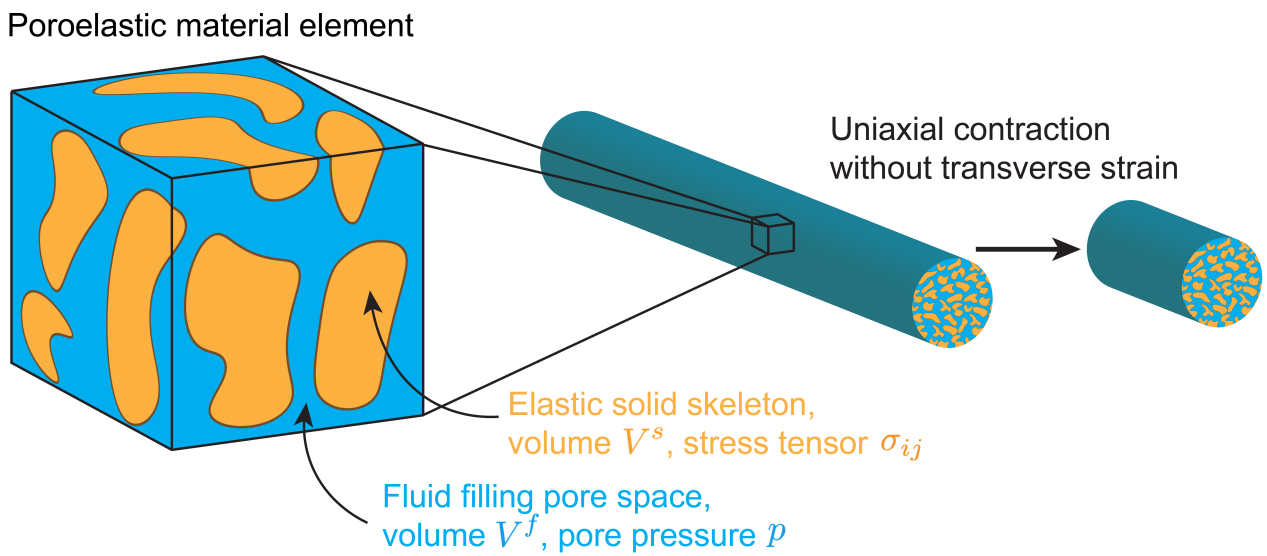


**Fig. S11. Poroelasticity.** Schematic diagram of a poroelastic volume element (left), as well as an illustration of uniaxial compression without transverse strain (right).

A volume element of a poroelastic material has fluid volume $V^f$ and solid volume $V^s$, and these together define the porosity

$$\phi = \frac{V_0^f}{V_0^s + V_0^f}, \qquad [36]$$

where the subscripts indicate their values in the initial undeformed configuration. For a homogeneous system $\phi$ is constant in space, and because it refers to the undeformed configuration it is also constant in time. The dynamical variables include the displacement of the solid skeleton $U_i^s$ and the displacement of the fluid $U_i^f$, from which we define the specific discharge of the fluid relative to the skeleton $Q_i = \phi(\partial_T U_i^f - \partial_T U_i^s)$. Here, the index $i = 1, 2, 3$ refers to the three Cartesian coordinates. From the motion of the solid skeleton, the symmetric strain tensor $\epsilon_{ij} = \frac{1}{2}(\partial_i U_j^s + \partial_j U_i^s)$ is formed. One also tracks $\zeta$, the variation in fluid volume per unit reference volume.

The internal energy of the poroelastic material can be written as a linear function of the kinematic "strain" variables $\epsilon_{ij}$ and $\zeta$ multiplied by their conjugate "stress" variables $\sigma_{ij}$ and $p$. The fluid pore pressure $p$ is the interpreted as the pressure of a hypothetical fluid reservoir in equilibrium with the immersed material element. The constitutive equation for the stress tensor $\sigma_{ij}$ of an isotropic poroelastic material can be written as (26, 27, 30, 31)

$$\sigma_{ij} = 2G_{\mathrm{M}}\epsilon_{ij} + \left(K_{\mathrm{M}} - \frac{2}{3}G_{\mathrm{M}}\right)\epsilon_{kk}\delta_{ij} - \alpha_{\mathrm{B}}\delta_{ij}p \qquad [37]$$

where $G_{\mathrm{M}}$ is the shear modulus, $K_{\mathrm{M}}$ is the bulk modulus, $\delta_{ij}$ is the Kronecker delta, and $\alpha_{\mathrm{B}}$ is Biot's effective stress constant, a parameter in the range $[0, 1]$ which captures the effect of the pore pressure on the elastic strain energy of the solid skeleton. Repeated indices imply summation, so that $\epsilon_{kk}$ is the trace of the solid skeleton strain tensor. The constitutive equation for the pore pressure is (26, 27, 30, 31)

$$\frac{\phi^2}{R}p = \zeta - \alpha_B\epsilon_{kk}, \qquad [38]$$

where $R$ is a material parameter with units of an elastic modulus. In Ref. 32, Eq. (38) is derived by accounting for the various factors affecting the proportional change $\zeta$ of fluid volume in a material element, and it reflects the fact that because $p$ is a pressure, it can only couple to the isotropic strain quantities $\epsilon_{kk}$ and $\zeta$ in the linear constitutive equations (26). See Ref. 33 for an interpretation of the parameters $\alpha_{\mathrm{B}}$ and $R$ in terms of microscopic properties of the material.

To study the dynamics of a poroelastic material, we next introduce the inertial force balance condition (30, 31)

$$\partial_j\sigma_{ij} + F_i^{\mathrm{b}} = \rho_s(1-\phi)\partial_T^2 U_i^s + \rho_f\phi\partial_T^2 U_i^f \qquad [39]$$

where $F_i^{\mathrm{b}}$ is a body force density, $\rho_s$ is the density of the solid skeleton, and $\rho_f$ is that of the fluid. Local continuity of the fluid also requires that (30, 31)

$$\partial_T\zeta + \partial_i Q_i = 0. \qquad [40]$$

These dynamical equations are closed using the dynamic version of Darcy's law, which reads (30, 31)

$$Q_i = -\kappa\left(\partial_i p + \frac{\rho_a}{\phi}\left(\partial_T^2 U_i^f - \partial_T^2 U_i^s\right) + \rho_f\partial_T^2 U_i^f\right), \qquad [41]$$

where $\kappa$ is a permeability constant that depends on the fluid viscosity and structural factors of the skeleton, and $\rho_a \propto \phi\rho_f$ is the apparent mass density.

**Extensions to incorporate the physics of myoneme networks** Eqs. (37) to (41) represent a closed system describing the poroelastodynamics of a material, and they can be rearranged as differential equations in the variables $U_i^s$ and $p$ (although other pairs of variables may be used in equivalent formulations). We now consider two extensions to these equations which represent additional physics in the myoneme-based system.

First, we allow for a non-autonomous active stretch tensor $g_{ij}$ which depends explicitly on space and time. It is also symmetric, i.e., $g_{ij} = g_{ji}$. The elastic restoring force of the solid skeleton should only depend on the relative strain tensor $\epsilon_{ij} - g_{ij}$, so we use this in place of the absolute strain tensor $\epsilon_{ij}$ where it appears in Eq. (37), which is now written as

$$\sigma_{ij} = 2G_{\mathrm{M}}\left(\epsilon_{ij} - g_{ij}\right) + \left(K_{\mathrm{M}} - \frac{2}{3}G_{\mathrm{M}}\right)\left(\epsilon_{kk} - g_{kk}\right)\delta_{ij} - \alpha_{\mathrm{B}}\delta_{ij}p. \quad [42]$$

As discussed in Ref. 32 where a similar "thermal strain" is considered in the context of soil dynamics, the constitutive equation for $p$, Eq. (38), is augmented to account for the variation in fluid volume due to the change in effective stress caused by the non-autonomous active stretch. We thus update Eq. (38) to

$$\frac{\phi^2}{R}p = \zeta - \alpha_B\epsilon_{kk} + \left(1 - \alpha_{\mathrm{B}}\right)g_{kk}. \quad [43]$$

Note that we are using displacement variables $U_i$ here, rather the position variables $X_i$ which are used in the main text. The two formulations are equivalent since the position variables can be recovered by adding the initial positions $X_i^0$ to the displacement variables. If the initial configuration defines the material coordinates, i.e., $X_i^0 = S_i$, one can show that the interpretation of $g_{ij}$ here is the same as that in the main text apart from an added constant term $g_{ij}^0 = \delta_{ij}$. Because derivatives of $g_{ij}$ and $U_i$ below enter in Eq. (45) and its approximations below, the constant term and the distinction between displacement and position can be neglected there.

Second, we allow for an additional external source of Stokes drag to act on the solid skeleton as a body force density $F_i^{\mathrm{b}} = -(\widetilde{\gamma}/A_i)\partial_T U_i^s$ where $\widetilde{\gamma}$ was introduced in *SI Appendix Supplementary methods* Section A and $A_i$ is a cross-sectional area perpendicular to the motion $U_i^s$. Our simple treatment of the drag as Stokesian and uniform along the system's length could be improved by introducing a memory kernel for the force history or by letting the drag $\mu$ be a function of position. However, it was found experimentally that the Stokesian drag dominates the contribution from the memory term in *Vorticella* (18), and we find here that a uniform $\mu$ still allows for excellent fits to experimental traces of length during contraction. The explicit dependence of drag on the organisms' shapes (i.e., cigar-shaped for *Spirostomum* and wine glass-shaped for *Vorticella*) could also be considered in future refinements of the model.

**Simplifying assumptions** The previous equations are not analytically tractable, so we now make two key approximations. First, we assume that the motion occurs only in the $x$-direction and does not produce transverse strain in the $y$ or $z$ directions. We let the cross-sectional area in the $yz$ plane be $A$, which we assume to be independent of $x$, and we denote the material coordinate in the $x$ direction as $S$. This motion, visualized in Figure S11, allows us to set $\epsilon_{11} = \partial_S U^s$ (where we dropped the subscript on $U_1^s$) and $g_{11} = g$ and all other elements of $\epsilon_{ij}$ and $g_{ij}$ to zero. Second, we assume that the static version of Darcy's law,

$$Q_i = -\kappa\partial_i p \quad [44]$$

can be used in place of the dynamic version in Eq. (41). The accuracy of this approximation improves if $\kappa$ is small, as discussed in Refs. 31 and 32.

Under these two approximations, we can write the dynamical equations for the displacement of the solid skeleton in the $x$-direction $U^s(S,T)$ and the pore pressure $p(S,T)$ as

$$\rho\partial_T^2 U^s = M_{\mathrm{M}}\left(\partial_S^2 U^s - \partial_S g\right) - \frac{\widetilde{\gamma}}{A}\partial_T U^s - \alpha_{\mathrm{B}}\partial_S p + \rho_f\kappa\partial_T\partial_S p \quad [45]$$

$$\frac{\phi^2}{R}\partial_T p = \kappa\partial_S^2 p - \alpha_{\mathrm{B}}\partial_T\partial_S U^s + \left(1 - \alpha_{\mathrm{B}}\right)\partial_T g. \quad [46]$$

where $M_{\mathrm{M}} = K_{\mathrm{M}} + 4G_{\mathrm{M}}/3$ is the p-wave modulus and $\rho = (1-\phi)\rho_s + \phi\rho_f$ is the bulk density. For a material whose Poisson ratio is zero, the p-wave modulus describing constrained uniaxial deformation is equal to the Young's modulus $E_{\mathrm{M}}$ for unconstrained uniaxial deformation, which for simplicity we assume holds here. In other words, we set $M_{\mathrm{M}} = E_{\mathrm{M}}$.

Eqs. (45) and (46) should be compared to Eq. (6) to understand the new physical ingredients due to poroelasticity. To put them in the form of Eq. (7), we write these new equations as

$$\partial_T^2 U^s = \alpha\left(\partial_S^2 U^s - \partial_S g\right) - \mu\partial_T U^s - a_1\partial_S f_p + a_2\partial_T\partial_S f_p \quad [47]$$

$$\partial_T f_p = a_3\partial_S^2 f_p - a_4\partial_T\partial_S U^s + a_5\partial_T g \quad [48]$$

where $f_p = pA$ is the force in the $x$ direction obtained by multiplying the pore pressure by the cross-sectional area $A$. We have also introduced the constants

$$\alpha = \frac{E_{\mathrm{M}}A}{\widetilde{m}} = \frac{E_{\mathrm{M}}}{\rho}, \quad \mu = \frac{\widetilde{\gamma}}{\widetilde{m}}$$

$$a_1 = \frac{\alpha_B}{\widetilde{m}}, \quad a_2 = \frac{\rho_f\kappa}{\rho A}, \quad a_3 = \frac{\kappa R}{\phi^2},$$

$$a_4 = \frac{A\alpha_{\mathrm{B}}R}{\phi^2}, \quad a_5 = \frac{A(1-\alpha_{\mathrm{B}})R}{\phi^2}$$

where $\widetilde{m} = m/\delta$ was introduced previously as the linear mass density of the spring chain. This is related to the volumetric bulk density through $\rho = \widetilde{m}/A = m/\delta A$.

**Analysis of poroelastic dynamics** Rather than attempt a bottom-up parameterization of the system to fix the seven parameters, we make one further approximation by assuming that both the fluid and solid skeleton are incompressible. This is known as the "incompressible constituents" assumption, and its implications in the context of cytoplasmic poroelasticity of eukaryotic cells (including its association with pressure diffusion dynamics) is described in Ref. 21. As detailed in Ref. 31, this assumption corresponds to $\alpha_{\mathrm{B}} = 1$, and we thus set $a_5 = 0$. It further corresponds to $R \to \infty$ (which can be shown to not affect setting $a_5 = 0$). This implies that the large terms proportional to $a_3$ and $a_4$ on the right-hand-side of Eq. (48) cause the poroelastic force $f_p$ to equilibrate rapidly with respect to the change in $U^s$. This is a quasi-steady state limit (34) for the dynamics of $f_p$, allowing us to set $\partial_T f_p = 0$. Eq. (48) then implies that

$$\partial_S f_p = \frac{a_4}{a_3}\partial_T U^s = \frac{A}{\kappa}\partial_T U^s. \tag{49}$$

Substituting this relation in Eq. (47) and setting the term proportional to $\partial_T \partial_S f_p$ to zero, we have

$$\partial_T^2 U^s = \alpha\left(\partial_S^2 U^s - \partial_S g\right) - \left(\mu + \frac{A}{\kappa\widetilde{m}}\right)\partial_T U^s. \tag{50}$$

In other words, for this limit the effect of poroelasticity is simply to add a term to the Stokesian drag on the motion of the solid skeleton. Under this limit, the scaling results obtained in the main text using the model without poroelasiticty still hold because the effective drag $\mu + A/\kappa\widetilde{m}$ is a linear function of the external drag $\mu$, having a constant additional contribution $A/\kappa\widetilde{m}$ which is determined by the permeability, density, and size of the organism's interior. We leave to future work a numerical exploration of Eqs. (47) and (48), where the incompressible constituents approximation is not made. Measuring the pororoelastic parameters for *Spirostomum* and considering models that account for transverse strain (which can be appreciable, as shown in Figure S3) are additional important directions for future work.

***C.3. Auxiliary elastic elements.*** Finally, we extend the model by including an auxiliary elastic element which passively resists compression caused by the $Ca^{2+}$-activated springs. This represents a simplified model for, for instance, the effect of the microtubule sheath in *Spirostomum* or the bent elastic stalk in *Vorticella* (4, 19).

In the discrete model, the force on the $i^{th}$ node becomes

$$\begin{aligned} m\partial_T^2 X_i = {} & k\left(X_{i+1} - X_i - G_{i+\frac{1}{2}}\right) - k\left(X_i - X_{i-1} - G_{i-\frac{1}{2}}\right) \\ & + k^*\left(X_{i+1} - X_i - G^*_{i+\frac{1}{2}}\right) - k^*\left(X_i - X_{i-1} - G^*_{i-\frac{1}{2}}\right) - \gamma\partial_T X_i \end{aligned} \tag{51}$$

where the starred parameters refer to a set of auxiliary springs acting in parallel to the active springs. We assume that the auxiliary spring rest lengths $G^*$ are uniform and constant in time. Passing to the continuum limit, we have

$$\partial_T^2 X - \alpha\left(\partial_S^2 X - \partial_S g\right) - \alpha^*\partial_S^2 X + \mu\partial_T X = 0 \tag{52}$$

which can be re-expressed as

$$\partial_T^2 X - \alpha_{\mathrm{tot}}\left(\partial_S^2 X - \beta\partial_S g\right) + \mu\partial_T X = 0 \tag{53}$$

where $\alpha_{\mathrm{tot}} = \alpha + \alpha^*$ and $\beta = \alpha/\alpha_{\mathrm{tot}} \in [0, 1]$. The force balance at the end of the chain imposes the boundary conditions

$$\partial_S X = \beta g + (1-\beta)g^*. \tag{54}$$

In the steady-state, we have

$$X(S) = \beta\int_0^S g(S')dS' + g_1 S + g_2. \tag{55}$$

The integration constant $g_2$ can be set to zero, and the boundary conditions imply that $g_1 = (1-\beta)\,g^*$. At long times, $g(S) = g_{\min}$, so that the steady-state is

$$X(S) = \left(\beta g_{\min} + (1-\beta)\,g^*\right)S. \tag{56}$$

The equilibrium shape is thus determined by a weighted combination of the stretches $g_{\min}$ and $g^*$ with the weights determined by the corresponding stiffness of the active and auxiliary springs.

We next ask whether the auxiliary springs affect the dynamical scaling results obtained without auxiliary springs, when $\alpha^* = 0$. By defining $\hat{X} = X/\beta$, we can map Eq. (53) into

$$\partial_T^2 \hat{X} - \alpha_{\mathrm{tot}}\left(\partial_S^2 \hat{X} - \partial_S g\right) + \mu\partial_T \hat{X} = 0, \tag{57}$$

which is formally identical to Eq. (7). The same logic leading to the scaling relationships for $\dot{\lambda}_{\max}$ obtained in the main text now carry through for $\dot{\hat{\lambda}}_{\max}$, which is defined using $\hat{X}$ (and $\hat{L}(T) = \hat{X}(L,T) - \hat{X}(0,T)$) in place of $X$. In the new scaling relations, $\alpha$ is replaced by $\alpha_{\mathrm{tot}}$ and $L$ is replaced by $\hat{L}$.

**D. Exact solution in the quench limit.** The solution to Eq. (15) in the main text can be found exactly using a Fourier expansion. The initial condition is expanded as

$$y(s,0) = a_0 + \sum_{n=1}^{\infty} a_n \cos(n\pi s), \quad [58]$$

where $a_0$ may be set to zero and

$$a_n = \int_0^1 y(s,0)\cos(n\pi s) ds. \quad [59]$$

By linearity, the solution can then be written as

$$y(s,t) = \sum_{n=1}^{\infty} a_n y_n(s,t). \quad [60]$$

The functions $y_n(s,t)$ can be found by solving Eq. (15) in the main text with the simplified initial conditions $y(s,0) = \cos(n\pi s)$, and the result is

$$y_n(s,t) = \cos(n\pi s) e^{-\frac{\eta_{m,d} t}{2}} \left( \cosh(t\psi_n/2) + \frac{\eta_{m,d} \sinh(t\psi_n/2)}{\psi_n} \right) \quad [61]$$

where

$$\psi_n = \sqrt{\eta_{m,d}^2 - 4n^2\pi^2}. \quad [62]$$

There is a similarity between the continuum quench model, whose dynamics are given in Eq. (15) of the main text, and perhaps the simplest dissipative contraction dynamics which one could consider: the motion of a single mass attached by a spring to a wall, following sudden release from an initial fixed state. The position of the mass $z(t)$ obeys

$$\partial_t^2 z + \omega^2 z + \mu \partial_t z = 0 \quad [63]$$

where $\omega = \sqrt{k/m}$ and $\mu = \gamma/m$ are defined in terms of the spring's stiffness $k$, mass $m$, and the drag coefficient $\gamma$. By rewriting $y_n(s,t)$ from Eq. (61) as

$$y_n(s,t) = \cos(n\pi s) z_n(t) \quad [64]$$

and using the solution of $y(s,t)$ from Eq. (60), one can show that Eq. (15) in the main text is equivalent to

$$\sum_{n=1}^{\infty} a_n \cos(n\pi s) \left( \partial_t^2 z_n(t) + (n\pi)^2 z_n(t) + \eta_{m,d} \partial_t z_n(t) \right) = 0, \quad [65]$$

which further implies that

$$\partial_t^2 z_n(t) + (n\pi)^2 z_n(t) + \eta_{m,d} \partial_t z_n(t) = 0 \quad [66]$$

for each $n$. Thus, in the continuum quench model, each spatial harmonic of the initial deviation from equilibrium behaves like a damped spring with frequency $n\pi$ and drag $\eta_{m,d}$.

**E. Energetics of contraction.** Here we consider the energetics of myoneme contraction. The elastic energy of the system is the sum of the energy of each spring in the chain. In the continuum limit this is (cf. Eq. (2))

$$U_{\mathrm{el}} = \frac{E_{\mathrm{M}} A}{2} \int_0^L (\partial_S X - g)^2 dS, \quad [67]$$

using dimensional variables. The non-dimensional version is

$$u_{\mathrm{el}} \equiv \frac{2U_{\mathrm{el}}}{E_{\mathrm{M}} A L} = \int_0^1 (\partial_s x - f)^2 ds = \int_0^1 h^2 ds, \quad [68]$$

where we have absorbed the factor $1/2$ into the definition of $u_{\mathrm{el}}$ for simplicity and used the definition of $h$ in Eq. (12) of the main text. Trajectories of $l(t)$ and $u_{\mathrm{el}}(t)$ are shown in *SI Appendix* Figure S1 for several values of the non-dimensional model parameters $\eta_{w,m}$ and $\eta_{w,d}$.

In the quench limit, the system starts at rest with $x = s$ and $f = 1$ and all springs then instantly take new rest lengths $g_{\min}$, causing the internal energy to jump discontinuously from $u_{\mathrm{el}} = 0$ to $(1 - g_{\min})^2$. We can regard $(1 - g_{\min})^2$ as the maximum internal energy that the system can store in response to a active stretch wave $g(s,t)$ taking values in $[g_{\min}, 1]$. Outside the quench limit, the system relaxes while the wave is traversing its length, and the maximum internal energy stored in the organism during the contraction trajectory $u_{\mathrm{el}}^{\max} \equiv \max_t u_{\mathrm{el}}(t)$ is less than $(1 - g_{\min})^2$. We can therefore quantify how quench-like the dynamics are using

$$\chi \equiv \frac{u_{\mathrm{el}}^{\max}}{(1 - g_{\min})^2} \in (0,1). \quad [69]$$

**Movie S1. Contraction of *Spirostomum*, along with output from the contour-tracking Morphometrics software used to measure the change in length over time.**

**Movie S2. Contraction of *Vorticella*, along with output from the contour-tracking Morphometrics software used to measure the change in length over time.**

**Movie S3. Contraction of *Spirostomum*, showing the original video footage, a thresholded version, and the output of the Morphometrics contour tracking software.**

## References


1. J Schindelin, et al., Fiji: an open-source platform for biological-image analysis. *Nat. Methods* **9**, 676–682 (2012).
2. T Ursell, et al., Rapid, precise quantification of bacterial cellular dimensions across a genomic-scale knockout library. *BMC Biol.* **15**, 1–15 (2017).
3. EG Chung, S Ryu, Stalk-length-dependence of the contractility of Vorticella convallaria. *Phys. Biol.* **14**, 066002 (2017).
4. G Misra, RB Dickinson, AJ Ladd, Mechanics of Vorticella contraction. *Biophys. J.* **98**, 2923–2932 (2010).
5. DC France, Ph.D. thesis (Massachusetts Institute of Technology) (2007).
6. S Schuster, M Marhl, T Höfer, Modelling of simple and complex calcium oscillations: From single-cell responses to intercellular signalling. *Eur. J. Biochem.* **269**, 1333–1355 (2002).
7. G Dupont, M Falcke, V Kirk, J Sneyd, *Models of Calcium Signalling.* (Springer), (2016).
8. K Katoh, M Kikuyama, An all-or-nothing rise in cytosolic. *J. Exp. Biol.* **200**, 35–40 (1997).
9. H Shiono, Y Naitoh, Cellular contraction precedes membrane depolarization in Vorticella convallaria. *J. Exp. Biol.* **200**, 2249–2261 (1997).
10. K Katoh, Y Naitoh, Control of cellular contraction by calcium in Vorticella. *J. Exp. Biol.* **189**, 163–177 (1994).
11. I Delvendahl, et al., Reduced endogenous $Ca^{2+}$ buffering speeds active zone $Ca^{2+}$ signaling. *Proc. Natl. Acad. Sci.* **112**, E3075–E3084 (2015).
12. SP Dawson, J Keizer, JE Pearson, Fire–diffuse–fire model of dynamics of intracellular calcium waves. *Proc. Natl. Acad. Sci.* **96**, 6060–6063 (1999).
13. J Keizer, GD Smith, S Ponce-Dawson, JE Pearson, Saltatory propagation of $Ca^{2+}$ waves by $Ca^{2+}$ sparks. *Biophys. J.* **75**, 595–600 (1998).
14. R Kupferman, PP Mitra, P Hohenberg, S Wang, Analytical calculation of intracellular calcium wave characteristics. *Biophys. J.* **72**, 2430–2444 (1997).
15. AJ Mathijssen, J Culver, MS Bhamla, M Prakash, Collective intercellular communication through ultra-fast hydrodynamic trigger waves. *Nature* **571**, 560–564 (2019).
16. VV Yashin, AC Balazs, Pattern formation and shape changes in self-oscillating polymer gels. *Science* **314**, 798–801 (2006).
17. S Shankar, L Mahadevan, Active muscular hydraulics. *bioRxiv* pp. 2022–02 (2022).
18. A Upadhyaya, et al., Power-limited contraction dynamics of Vorticella convallaria: an ultrafast biological spring. *Biophys. J.* **94**, 265–272 (2008).
19. L Xu, M Bhamla, Biophysical mechanism of ultrafast helical twisting contraction in the giant unicellular ciliate Spirostomum ambiguum. *bioRxiv* p. 854836 (2019).
20. GT Charras, TJ Mitchison, L Mahadevan, Animal cell hydraulics. *J. Cell Sci.* **122**, 3233–3241 (2009).
21. E Moeendarbary, et al., The cytoplasm of living cells behaves as a poroelastic material. *Nat. Mater.* **12**, 253–261 (2013).
22. R Chang, M Prakash, Entangled architecture of rough endoplasmic reticulum (RER) and vacuoles enables topological damping in cytoplasm of an ultra-fast giant cell. *bioRxiv* (2021).
23. J Zhang, et al., Giant proteins in a giant cell: Molecular basis of ultrafast ca2+-dependent cell contraction. *Sci. Adv.* **9**, eadd6550 (2023).
24. T Healey, Material symmetry and chirality in nonlinearly elastic rods. *Math. Mech. Solids* **7**, 405–420 (2002).
25. J Gore, et al., DNA overwinds when stretched. *Nature* **442**, 836–839 (2006).
26. MA Biot, General theory of three-dimensional consolidation. *J. Appl. Phys.* **12**, 155–164 (1941).
27. MA Biot, DG Willis, The elastic coefficients of the theory of consolidation. *J. Appl. Mech.* **24**, 594–601 (1957).
28. JM Skotheim, L Mahadevan, Physical limits and design principles for plant and fungal movements. *Science* **308**, 1308–1310 (2005).
29. Y Forterre, JM Skotheim, J Dumais, L Mahadevan, How the venus flytrap snaps. *Nature* **433**, 421–425 (2005).
30. M Schanz, AD Cheng, Transient wave propagation in a one-dimensional poroelastic column. *Acta Mech.* **145**, 1–18 (2000).
31. M Schanz, Poroelastodynamics: linear models, analytical solutions, and numerical methods. *Appl. Mech. Rev.* **62** (2009).
32. O Zienkiewicz, T Shiomi, Dynamic behaviour of saturated porous media; the generalized Biot formulation and its numerical solution. *Int. J. for Numer. Anal. Methods Geomech.* **8**, 71–96 (1984).
33. E Detournay, AHD Cheng, Fundamentals of poroelasticity in *Analysis and Design Methods.* (Elsevier), pp. 113–171 (1993).
34. RA Bond, BS Martincigh, JR Mika, RH Simoyi, The quasi-steady-state approximation: Numerical validation. *J. Chem. Ed.* **75**, 1158 (1998).